2019

Spin filtering in CrI3 tunnel junctions

T. R. Paudel and E. Y. Tsymbal

ACS APPLIED MATERIALS & INTERFACES

Research Article

Cite This: ACS Appl. Mater. Interfaces 2019, 11, 15781−15787

www.acsami.org

Spin Filtering in CrI_3 Tunnel Junctions

Tula R. Paudel* and Evgeny Y. Tsymbal*

Department of Physics and Astronomy & Nebraska Center for Materials and Nanoscience, University of Nebraska, Lincoln, Nebraska 68588, United States

Supporting Information

ABSTRACT: The recently discovered magnetism of two-dimensional (2D) van der Waals crystals has attracted a lot of attention. Among these materials is CrI_3, a magnetic semiconductor, exhibiting transitions between ferromagnetic and antiferromagnetic orderings under the influence of an applied magnetic field. Here, using first-principles methods based on density functional theory, we explore spin-dependent transport in tunnel junctions formed of face-centered cubic Cu(111) electrodes and a CrI_3 tunnel barrier. We find about 100% spin polarization of the tunneling current for a ferromagnetically ordered four-monolayer CrI_3 and a tunneling magnetoresistance of about 3000% associated with a change of magnetic ordering in CrI_3. This behavior is understood in terms of the spin and wave-vector-dependent evanescent states in CrI_3, which control the tunneling conductance. We find a sizable charge transfer from Cu to CrI_3, which adds new features to the mechanism of spin filtering in CrI_3-based tunnel junctions. Our results elucidate the mechanisms of spin filtering in CrI_3 tunnel junctions and provide important insights for the design of magnetoresistive devices based on 2D magnetic crystals.

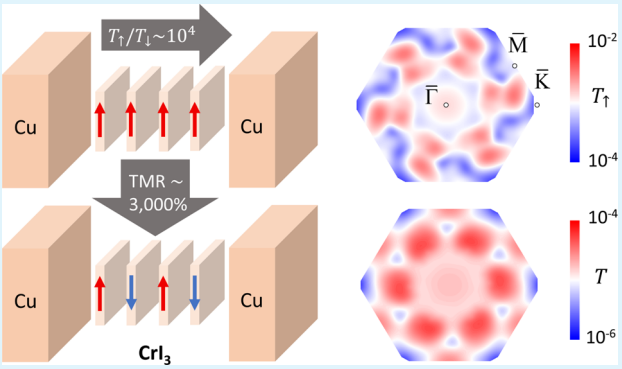

KEYWORDS: *CrI_3, 2D magnet, tunnel junction, spin filtering, tunneling magnetoresistance, DFT calculations*

INTRODUCTION

The growing family of two-dimensional (2D) materials offers a platform to design novel van der Waals heterostructures with unique electronic and optical properties.[1,2] Recently, the range of these properties has been expanded to include 2D magnetism.[3−5] Although a magnetic order is prohibited within the 2D isotropic Heisenberg model at finite temperatures,[6] magnetocrystalline anisotropy lifts this restriction and enables the appearance of 2D Ising ferromagnetism. The discovery of long-range magnetic order in 2D crystals, such as CrI_3,[3] opens a new route for the fundamental studies of spin behavior at low dimensions and could lead to novel spintronics applications.

CrI_3 is a semiconductor with easily exfoliating monolayers. The van der Waal's force binds stiff CrI_3 monolayers with a cleavage energy comparable to that of transition metal chalcogenides and graphene.[7,8] Bulk CrI_3 is a ferromagnet with the Curie temperature of 61 K, the magnetic moment of $3.1\mu_B$ per Cr atom[9] being oriented out of the layer plane with a magnetic anisotropy of about 650 μeV.[10] When exfoliated, CrI_3 exhibits a magnetic order dependent on layer thickness: whereas a CrI_3 monolayer is an Ising ferromagnet, a CrI_3 bilayer is an antiferromagnet consisting of two ferromagnetic (FM) monolayers with antiparallel magnetic moments.[3] Under an applied magnetic field of $0.65T$,[3] a CrI_3 bilayer exhibits a spin-flip transition, which changes the interlayer magnetic alignment from antiferromagnetic (AFM) to FM. This indicates a relatively weak interlayer exchange coupling of about 0.2 meV, which allows tuning the spin-flip transition by electric means.[11,12] The switching of the magnetic order in CrI_3 from AFM to FM has recently been demonstrated by the electric field effect[13] and electrostatic doping[11,14] under a constant magnetic bias.

The existence of magnetism in CrI_3, which can be engineered in a layer-by-layer fashion, expands the functional properties of the 2D materials. It makes possible to design van der Waal's heterostructures combining magnetic and non-magnetic components where the electrical and optical properties can be controlled by the magnetic ordering of the adjacent layers. A prominent example is a large tunneling magnetoresistance (TMR) effect of 95, 300, and 550%, which was reported for graphite/CrI_3/graphite tunnel junctions with bilayer, trilayer, and tetralayer CrI_3 barriers, respectively.[15] Here, CrI_3 served as a tunneling barrier and TMR was associated with a change of magnetic ordering of CrI_3 from AFM to FM under the influence of an applied magnetic field. This is different from the conventional TMR effect in magnetic tunnel junctions where two FM electrodes are realigned by an applied magnetic field, resulting in a change of tunneling resistance,[16] and the related effects in ferroelectric tunnel junctions with magnetic electrodes.[17,18] Even higher values of TMR were demonstrated for other types of tunnel junctions

Received: February 6, 2019
Accepted: April 8, 2019
Published: April 9, 2019

DOI: 10.1021/acsami.9b01942
ACS Appl. Mater. Interfaces 2019, 11, 15781−15787

utilizing CrI_3 barrier layers of different thicknesses: 19 000%,[19] 10 000%,[20] and even 1 000 000%[21] at a finite bias voltage.

The appearance of the giant TMR effect in tunnel junctions based on CrI_3 barriers is understood in terms of the spin-filtering effect.[14−20] According to the density functional theory (DFT) calculations, the conduction band of CrI_3 is fully spin-polarized[7,22] so that the band gap for majority-spin electrons is smaller than that for minority-spin electrons. This creates a spin-dependent tunneling barrier which filters electrons according to their spin orientation. Therefore, when the CrI_3 monolayers are FM-ordered under the influence of a sufficiently large magnetic field, the tunneling current is dominated by majority-spin electrons, which encounter a low tunneling barrier, and hence, the conductance is high. However, when the CrI_3 monolayers are AFM-ordered at zero magnetic field, both majority- and minority-spin electrons encounter a higher barrier, whose height varies across the CrI_3 layer, and the conductance is low. Note that the detection of the spin-filtering effect in CrI_3-based tunnel junctions is different from that in the conventional spin-filter tunnel junctions, where a FM counter electrode is required to select the tunneling spins.[23,24]

Although the mechanism of the giant TMR in CrI_3-based tunnel junctions has been articulated qualitatively, the quantitative analysis and detailed physical understanding of the spin-filtering effect are still missing. In this paper, we employ DFT calculations to elucidate the spin-dependent transport properties of the tunnel junctions, which consist of face-centered cubic (fcc) Cu(111) electrodes and a magnetic CrI_3 barrier layer. Cu as an electrode material was chosen because of a small lattice mismatch with CrI_3, a simple free-electron-like Fermi surface, and appropriate band alignment placing the Cu Fermi level within the band gap of the CrI_3. We find a nearly 100% spin polarization of the tunneling current for ferromagnetically ordered CrI_3 and a giant TMR effect increasing with CrI_3 thickness. This behavior is explained in terms of the spin and wave-vector-dependent evanescent states in CrI_3, which control the tunneling conductance. In addition, we find a sizable charge transfer from Cu to CrI_3, which adds a new feature to the mechanism of spin filtering in CrI_3-based tunnel junctions, as compared to those utilizing graphite electrodes.

RESULTS

Bulk CrI_3. Bulk CrI_3 in the hexagonal setting of space group 148 ($R\bar{3}$) contains three CrI_3 layers stacked in the [0001] direction as shown in Figure 1a. Figure 1c,d shows the calculated band structure of bulk CrI_3 along the high-symmetry directions in the 3D Brillouin zone (Figure 1b) for AFM (Figure 1c) and FM (Figure 1d) CrI_3. The calculated energy gap is 0.92 eV for FM and 1.05 eV for AFM configuration. Both values are smaller than the measured band gap of 1.2 eV,[9] which is due to the well-known deficiency of the standard DFT approach.[25] The energy position and the orbital character of the conduction band minimum (CBM) control the transport properties of CrI_3. The band structure of CrI_3 is determined by the crystal field splitting of the 3d orbitals of the Cr^{3+} ion ($[Ar]\,3d^3$) located at the center of the octahedron formed by the six I^{-1} ions (Figure 1a). The crystal field of octahedral symmetry breaks the Cr 3d orbital state into the triply degenerate t_{2g} state, which lies at a lower energy, and the doubly degenerate e_g state, which lies at a higher energy. According to Hund's rule, the majority-spin t_{2g} states are fully occupied by the three

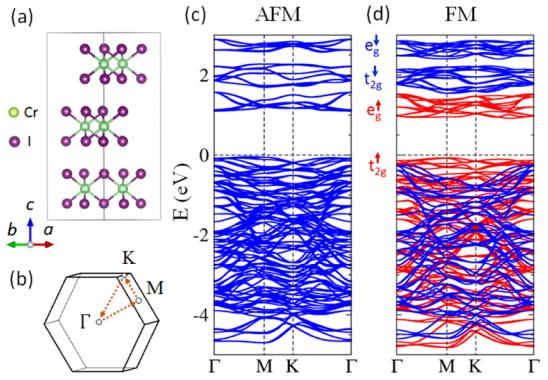

Figure 1. Atomic and electronic structure of bulk CrI_3. Atomic structure of the unit cell of bulk CrI_3 (a) and the corresponding Brillouin zone with the high-symmetry points indicated (b). Spin-projected band structure of bulk FM (c) and AFM (d) CrI_3 calculated along the high-symmetry lines indicated in (b) with the Cr orbital character for selected bands shown. Red (blue) color designates the majority (minority)-spin bands.

available Cr^{+3} electrons and form the valence band, whereas the minority-spin t_{2g} states and the e_g states are empty and form the conduction band (Figure 1d). The exchange splitting of the spin bands makes the band gap in CrI_3 spin-dependent. While the majority-spin CBM is formed of the e_g states and lies at about 1 eV above the valence band maximum (VBM), the minority-spin CBM is formed of the t_{2g} states and lies at about 1.6 eV above the VBM (Figure 1d). The spin-dependent band gap is responsible for the spin-dependent barrier height in tunnel junctions based on CrI_3, which is the origin of the spin-filtering effect.

Cu/CrI_3/Cu Tunnel Junction: Atomic Structure. We consider a Cu/CrI_3/Cu tunnel junction which consists of a four-monolayer CrI_3(001) tunnel barrier stacked according to the bulk $R\bar{3}$ symmetry and placed between five monolayers of Cu(111) as shown in Figure 2a. We assume the in-plane

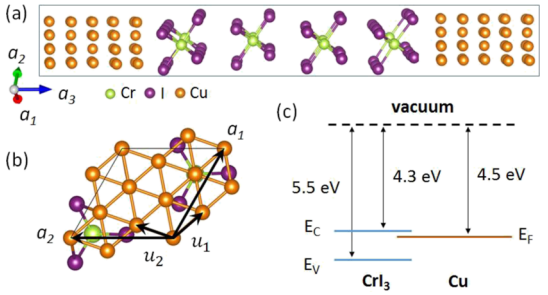

Figure 2. Side (a) and top (b) views of the atomic structure of the Cu(5ML)/CrI_3(4ML)/Cu(5ML) tunnel junction. (c) Band alignment between bulk CrI_3(001) and fcc Cu(111).

constant of the supercell to be the theoretical bulk lattice constant of CrI_3, a = 6.81 Å (the reported experimental value is 6.87 Å[8]). In the supercell, the lattice vectors of CrI_3 slab are $\vec{a}_1 = (a/2, \sqrt{3}a/2, 0)$, $\vec{a}_2 = (a/2, -\sqrt{3}a/2, 0)$, and $\vec{a}_3 = (0,0,c)$, which represent the unit cell of bulk hexagonal CrI_3. To match the fcc Cu electrodes to the CrI_3 slab, we enlarge the in-plane Cu lattice parameters to be $\vec{a}_1 = 3\vec{u}_1 + \vec{u}_2$ and $\vec{a}_2 = 2\vec{u}_2 - \vec{u}_1$, where $\vec{u}_1$ and $\vec{u}_2$ are the unit vectors in the Cu(111) plane (Figure 2b). The estimated in-plane strain between Cu and CrI_3 slabs is $\epsilon_{11} = \epsilon_{22} \approx 1\%$,[26] suggesting possibility of good

DOI: 10.1021/acsami.9b01942
ACS Appl. Mater. Interfaces 2019, 11, 15781−15787

epitaxy. The Cu slab is positioned in such a way that one of the Cu atoms lies directly above the Cr atom, as shown in Figure 2b, so that it has the same distance from the nearest I atoms.

Calculations are performed as described in Methods. The atomic relaxation involves two steps. First, we find the minimum-energy distance, d_{min}, between the Cu(111) slab strained to the CrI_3(001) lattice constants and the CrI_3(001) slab, while keeping all the internal coordinates fixed, corresponding to bulk CrI_3 and Cu. Then, we fix d_{min} and relax all the atomic coordinates in the Cu/CrI_3/Cu supercell. We find that at the interface Cu and I atoms form bonds with the bond length of 2.67 Å. This is not surprising, as iodine is known to form compounds with the noble metals, such as Pt, Au, and Ag. In addition, the relaxation slightly reduces the interlayer spacing between the CrI_3 monolayers to 6.43 Å, as compared to the calculated bulk value of 6.46 Å (the reported experimental value is 6.60 Å[8]). It also makes the Cr−I bonds asymmetric with a longer bond of 2.77 Å next to the interface and a shorter of 2.69 Å bond away from the interface, as compared to the bulk Cr−I bond length of 2.71 Å. These bonds are largely symmetric in the middle CrI_3 monolayers. A tunnel junction with a two-monolayer CrI_3 barrier shows similar relaxation behavior.[27]

Cu/CrI_3/Cu Tunnel Junction: Electronic Structure. The electronic and transport properties of the Cu/CrI_3/Cu tunnel junction depend critically on the band offset between CrI_3 and Cu. Hence, we first calculate the band offset by analyzing the relative positions of the Fermi level in the Cu(111) slab and the VBM in the CrI_3(001) slab when the vacuum potentials of the two slabs are matched. Figure 2c shows that the Fermi level in Cu(111) lies about 0.2 eV below the CBM of CrI_3, indicating that the CrI_3 layer is expected to produce a tunneling barrier when used in a Cu/CrI_3/Cu tunnel junction.

This fact agrees with the calculated layer-resolved density of states (DOS) for a Cu/CrI_3/Cu tunnel junction with four monolayers of CrI_3 (Figure 2a). As seen from Figure 3a,b, away from the interface, the Fermi level lies within the band gap of CrI_3 for both FM- (Figure 3a) and AFM-ordered (Figure 3b) CrI_3. Therefore, a tunnel barrier exists for both majority- and minority-spin electrons. However, the height of the barrier and its profile across the Cu/CrI_3/Cu tunnel junction are spin-dependent and different for FM- and AFM-ordered CrI_3. In the FM configuration, there is a uniform barrier across the junction with the spin-dependent barrier height of about 0.2 eV in the majority-spin channel and about 0.8 eV in the minority-spin channel (Figure 3c). In this case, the transmission is expected to be large and dominated by majority-spin electrons. In the AFM configuration, the barrier height changes between low and high values on each consecutive CrI_3 monolayer for both spin channels (Figure 3d). In this case, the conductance is expected to be low in each spin channel and largely spin independent because of the mirror symmetry of the barrier profiles between the two spin channels.

There is another important feature in the electronic structure of the Cu/CrI_3/Cu tunnel junction. There is a sizable charge transfer from Cu to the first monolayer of CrI_3 at the Cu/CrI_3 interface. This is evident from the Fermi energy located within the majority-spin e_g conduction band of the interfacial CrI_3 monolayer (Figure 2a). Such an electron doping effect makes this CrI_3 monolayer "half-metallic", so that the majority-spin carriers experience no barrier within this monolayer (Figure 3c, top panel). This feature of the

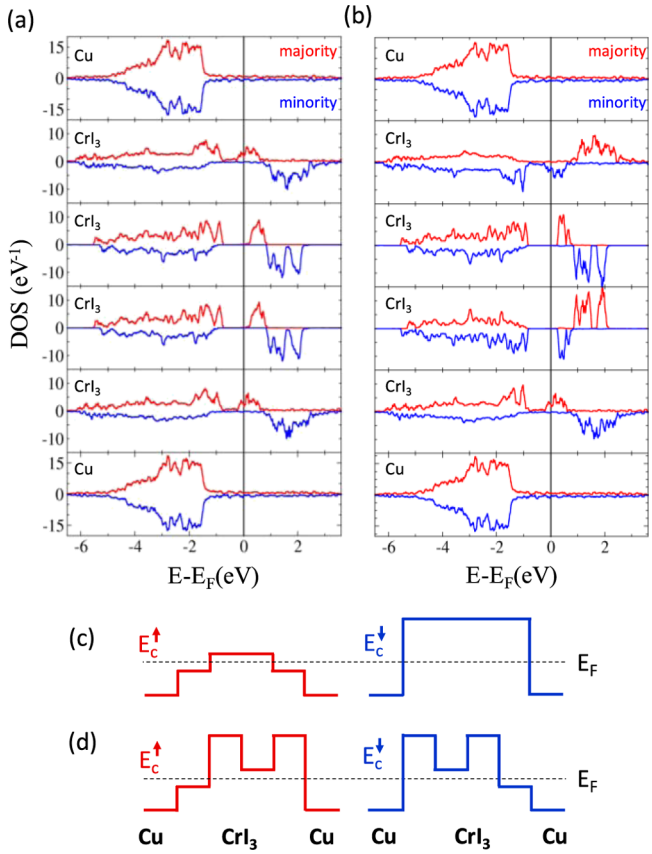

Figure 3. (a,b) Calculated layer- and spin-resolved DOS in a Cu(5ML)/CrI_3(4ML)/Cu(5ML) tunnel junction as a function of energy for FM- (a) and AFM- (b) ordered CrI_3. Top and bottom panels display DOS of the interfacial Cu MLs, and central panels display DOS of the four CrI_3 MLs. Majority (minority)-spin DOS is indicated by red (blue) lines. (c,d) Schematics of the spin-dependent potential barrier profile across the junction for FM- (c) and AFM- (d) ordered CrI_3. Majority (minority)-spin channels are indicated by red (blue) lines. The Fermi energy (E_F) is indicated by the dashed line.

electronic band structure at the Cu/CrI_3 interface adds additional contribution to the spin-filtering effect, as discussed below. For a two-monolayer CrI_3 tunnel junction, this "half-metallic" behavior becomes dominating and results in a large TMR of ~1500%.[27]

Cu/CrI_3/Cu Tunnel Junction: Transmission. The transmission function is calculated as described in Methods by considering the Cu/CrI_3/Cu(111) supercell (Figure 2a) as the scattering region ideally attached on both sides to semi-infinite Cu(111) electrodes. Figure 4a shows the calculated spin-resolved transmission $T_\sigma(E)$ ($\sigma = \uparrow, \downarrow$) across the FM-ordered Cu/CrI_3/Cu tunnel junction as a function of energy. There are several orders of magnitude difference in the transmission values between the majority- and minority-spin conduction channels over the whole range of energies. Relevant to experiment, the transmission value at the Fermi energy $T_\sigma(E_F)$ is 4 orders of magnitude higher for the majority-spin electrons as compared to the minority-spin electrons. The spin polarization of the tunneling conductance SP = $(T_\uparrow - T_\downarrow)/(T_\uparrow + T_\downarrow)$ is virtually 100%. This manifests a perfect spin-filtering effect resulting from the spin-dependent potential barrier in CrI_3 (Figure 3c).

Spin filtering is also responsible for the large TMR effect associated with the change in the magnetic ordering of CrI_3 by

DOI: 10.1021/acsami.9b01942
ACS Appl. Mater. Interfaces 2019, 11, 15781−15787

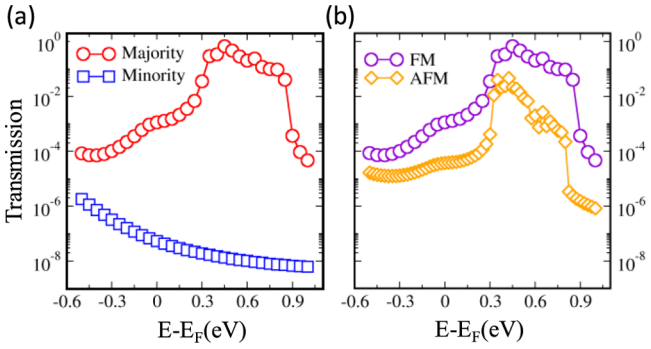

Figure 4. Spin-resolved transmission per lateral unit cell area across the Cu/CrI_3/Cu tunnel junction as a function of energy for FM-ordered CrI_3 (a) and total transmission for FM- and AFM-ordered CrI_3 (b).

an applied magnetic field. For FM-aligned CrI_3, the total transmission, $T_{FM} = T_\uparrow + T_\downarrow$, is nearly the same as the majority-spin transmission $T_\uparrow$ (due to $T_\uparrow \gg T_\downarrow$), which is shown in Figure 4a by red dots. For AFM-aligned CrI_3, the total transmission, T_{AFM}, is twice that per spin (due to symmetry of the considered tunnel junction making the spin transmission for each spin channel to be equal), which is shown in Figure 4b. By comparing Figure 4a,b, it is seen that T_{AFM} as a function of energy exhibits similar features as T_{FM}, but T_{AFM} is more than an order of magnitude lower than T_{FM} over the whole range of energies. This is explained by the spin-dependent potential profiles shown in Figure 3c,d for the FM- and AFM-ordered tunnel junction, respectively. While T_{FM} is dominated by the majority-spin electrons encountering a low potential barrier across the whole CrI_3 layer (Figure 3c, top panel), the AFM ordering makes the tunneling barrier high for either spin channel in those regions where the tunneling electrons have their spin antiparallel to the magnetic moment of the CrI_3 monolayer (Figure 3d). Thus, although the spin filtering selects a highly transmittive majority-spin channel for the FM configuration, it suppresses the transmission in either spin channel for the AFM configuration by the consecutive filtering of the majority- and minority-spin carriers when they are tunneling across the barrier. The TMR value calculated at the Fermi energy (corresponding to the low bias voltage regime) is $(T_{FM} - T_{AFM})/T_{AFM} \approx 3000\%$, which reveals a very large TMR effect in line with the experimental observations.[14−20]

As seen from Figure 4a,b, the spin filtering and TMR effects become even larger at higher energies. At about 0.3 eV above the Fermi energy, the majority-spin transmission across the FM-ordered CrI_3 is strongly enhanced (Figure 4a). A similar feature is seen for transmission across the AFM-ordered CrI_3 (Figure 4b). This behavior is due to the electron energy entering the majority-spin conduction band of CrI_3. At these energies, the enhanced spin filtering and TMR result from the essentially "metallic" conduction of the majority-spin electrons, in contrast to the tunneling conduction of the minority-spin electrons. The predicted enhancement of the spin filtering at higher energies is likely responsible for the experimentally observed enhancement of TMR with applied bias voltage.[3,18,20] Similar behavior is predicted for a tunnel junction with a two-monolayer CrI_3 barrier (Figure S1).

To obtain a deeper insight into the mechanism of spin-dependent tunneling, we calculate transmission $T(\mathbf{k}_\parallel)$ for different wave vectors $\mathbf{k}_\parallel$ in the 2D Brillouin zone. Because of periodicity of the system in the plane perpendicular to the transport direction, wave vector $\mathbf{k}_\parallel$ in that plane is conserved during the tunneling process. Figure 5a−c shows the calculated $\mathbf{k}_\parallel$-resolved transmission across the Cu/CrI_3/Cu tunnel junction for FM- (Figure 5a,b) and AFM- (Figure 5c) aligned CrI_3. As is seen from the figures; in all cases, the transmission is

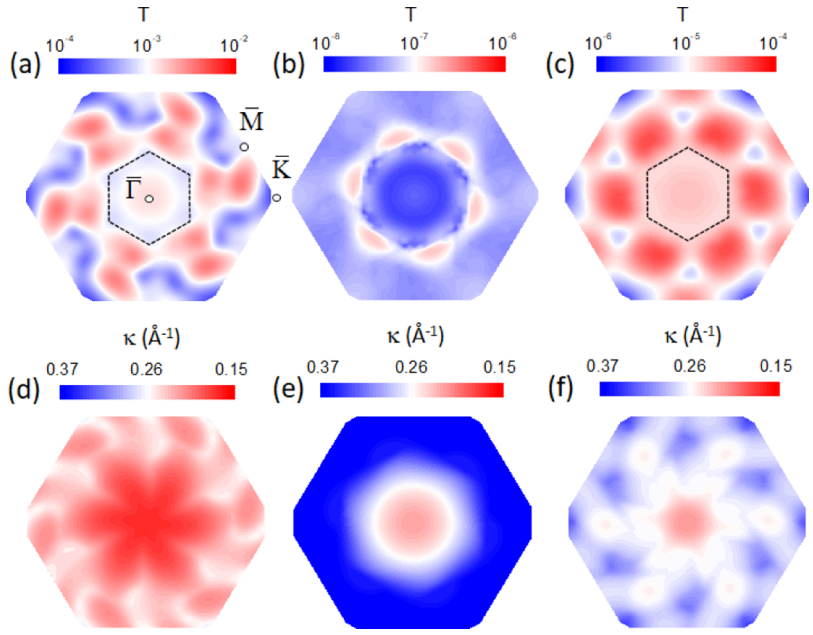

Figure 5. (a−c) $\mathbf{k}_\parallel$-resolved transmission (T) across the Cu/CrI_3/Cu tunnel junction in the 2D Brillouin zone for majority (a) and minority (b) spins for FM- and AFM- (c) ordered CrI_3, respectively. The transmission is plotted in a logarithmic scale [note different scales for (a−c)]. The high-symmetry points in the 2D Brillouin zone are shown. Dashed lines in (a−c) indicate the region where there are no available propagating states in the interface monolayer of CrI_3. (d−f) $\mathbf{k}_\parallel$-resolved lowest decay rate for majority (a) and minority (b) spins for FM- and AFM- (c) ordered bulk CrI_3 calculated at 0.2 eV below the CBM.

DOI: 10.1021/acsami.9b01942
ACS Appl. Mater. Interfaces 2019, 11, 15781−15787

slightly reduced around the high-symmetry $\bar{\Gamma}$ point and enhanced in certain peripheral regions of the 2D Brillouin zone.

In order to understand this behavior, we analyze the complex band structure of bulk CrI_3. It is known that tunneling through insulators can be interpreted in terms of evanescent states,[28] and the method to investigate them is the complex band structure in the energy gap region.[29−31] To obtain the complex band structure, for each $\mathbf{k}_{||}$, we calculate the dispersion relation $E = E(k_z)$, allowing complex $k_z = q + i\kappa$. The imaginary part κ is the decay rate so that the corresponding wave functions decay as $\sim e^{-\kappa z}$. The evanescent states with the lowest decay rate are expected to be most efficient in the tunneling process and hence to control the transmission. In Figure 5d−f, we plot the lowest decay rate $\kappa(\mathbf{k}_{||})$ for the energy in the band gap of bulk CrI_3, corresponding to the Fermi energy in the Cu/CrI_3/Cu tunnel junction. Below, we discuss the relationship between the $\mathbf{k}_{||}$-dependent transmission (Figure 5a−c) and the lowest decay rate (Figure 5d−f).

First, we consider the majority-spin conduction channel for the FM-aligned CrI_3. By comparing Figure 5a,d, we see that away from $\bar{\Gamma}$ point closer to the edges of the 2D Brillouin zone (beyond the hexagon indicated by the dashed line in Figure 5a), there is a clear resemblance between the high values of $T(\mathbf{k}_{||})$ and the low decay rates $\kappa(\mathbf{k}_{||})$. This behavior is consistent with the expectation that the slowest decaying evanescent states produce the highest transmission. However, the six-petal flower feature with the lowest decay rate centered at the $\bar{\Gamma}$ point seen in the color plot of $\kappa(\mathbf{k}_{||})$ (Figure 5d) is not reproduced in the color plot of $T(\mathbf{k}_{||})$ (Figure 5a).

This behavior can be understood in terms of the $\mathbf{k}_{||}$-dependent DOS at the interfacial monolayer of CrI_3. As was discussed in conjunction with the DOS plotted in Figure 3a, due to the charge transfer from Cu, this monolayer of CrI_3 has a nonzero majority-spin DOS at the Fermi energy and thus serves as the termination of the metal electrode rather than a tunneling barrier. The $\mathbf{k}_{||}$-dependent DOS determines the efficiency of transmission across this monolayer from the Cu electrode further into the tunneling region of CrI_3. Figure 6a shows the $\mathbf{k}_{||}$-dependent majority-spin DOS of bulk CrI_3 at E = 0.23 eV above the CBM corresponding to the Fermi energy in the interfacial CrI_3 monolayer (see Figure 3a). The key feature of this plot is the absence of electronic states within the hexagonal region around the $\bar{\Gamma}$ point. Thus, while the electronic states are available in the most peripheral region of the 2D Brillouin zone, supporting the metallic-like transmission across this area, there are no propagating states in the central hexagonal region, which implies that the transmission though this area is suppressed. This fact explains the reduced transmission seen within the hexagonal region in Figure 5a, indicated by the dashed line. The similar behavior is observed for the Cu/CrI_3(2ML)/Cu tunnel junction (Figure S1d). The six-petal flower feature, showing the lowest decay rates in CrI_3 (Figure 5d), reveals itself only at the edges of the petals where the enhanced transmission is seen in Figure 5a.

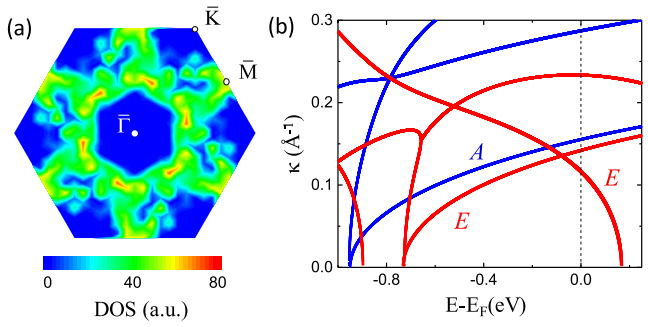

Figure 6. (a) $\mathbf{k}_{||}$-resolved majority-spin DOS of bulk FM-ordered CrI_3 plotted in the 2D Brillouin zone at E = 0.23 eV above the CBM. (b) Complex band structure of CrI_3 for majority- (red curves) and minority- (blue curves) spin electrons. The dashed line indicates the Fermi energy in the Cu/CrI_3/Cu tunnel junction.

For AFM-ordered CrI_3, the $\mathbf{k}_{||}$-resolved transmission across the Cu/CrI_3/Cu tunnel junction (Figure 5c) shows a qualitatively similar behavior, although it is lower by about 2 orders in magnitude than the transmission for FM-ordered CrI_3. By comparing Figure 5c,f, we see a qualitative similarity between the high values of $T(\mathbf{k}_{||})$ and the low decay rates $\kappa(\mathbf{k}_{||})$ in the peripheral region of the 2D Brillouin zone. The transmission is suppressed however within the hexagonal area (indicated by the dashed line in Figure 5c) because of the absence of electronic states at one of the interfaces (left or right depending on the spin channel) in this region of the Brillouin zone (Figure 6a).

The situation is different for the minority-spin transmission $T(\mathbf{k}_{||})$ across the FM-ordered Cu/CrI_3/Cu tunnel junction. First, as seen from Figure 5b, the transmission values are about 4 orders in magnitude smaller than those for the majority spin (Figure 5a). Second, there is virtually no correlation between $T(\mathbf{k}_{||})$ and $\kappa(\mathbf{k}_{||})$. According to Figure 5e, the expected high transmission should occur at the $\bar{\Gamma}$ point. However, as seen from Figure 5b, transmission is suppressed in the hexagonal area around this point. This disparity is due to the symmetry mismatch between the states available at the Fermi energy in Cu and the evanescent states in CrI_3 at the $\bar{\Gamma}$ point. This can be understood from Figure 6b, where we plot the imaginary part of the wave vector κ in bulk CrI_3 as a function of energy at the $\bar{\Gamma}$ point. There are several majority- and minority-spin evanescent bands crossing the Fermi energy (indicated by the vertical dashed line in Figure 6b). The states with the lowest decay rate have the E symmetry representation for the majority-spin electrons and the A symmetry representation for the minority-spin electrons, corresponding to the group of the wave vector along the $\Gamma-Z$ direction in the Brillouin zone of bulk CrI_3. In terms of atomic orbitals, the A symmetry state transforms as s, p_z, and d_{z^2} orbitals, whereas the E symmetry state transforms as p_x, p_y, $d_{x^2-y^2}$, d_{xy}, d_{yz}, and d_{xz} orbitals. The incoming Cu states at the $\bar{\Gamma}$ point contain the mixture of the Cu s, p, and d atomic orbitals; however, the contribution of the A symmetry states is much smaller (~5%) compared to the contribution of the E symmetry states. Thus, the symmetry mismatch between the incoming and evanescent states suppresses the transmission around the $\bar{\Gamma}$ point and makes the overall transmission of the minority-spin electrons low.

SUMMARY

Using first-principles methods based on density functional theory (DFT), we have explored the mechanisms of the spin-filtering effect in tunnel junctions with a 2D FM insulator CrI_3 used as a tunneling barrier. Our results demonstrate that a four-monolayer CrI_3 barrier provides virtually a fully spin-polarized transmission in a tunnel junction utilizing fcc Cu(111) electrodes. The predicted TMR effect is about 5000%, associated with the change of magnetic ordering in CrI_3 from FM to AFM. A simple qualitative picture of the spin-

DOI: 10.1021/acsami.9b01942
ACS Appl. Mater. Interfaces 2019, 11, 15781−15787

filtering effect is based on the exchange splitting of the spin bands in CrI_3 producing different barrier heights for majority- and minority-spin carriers. The detailed analysis of the spin-dependent electronic band structure and the spin and wave-vector-resolved transmission in $Cu/CrI_3/Cu$ tunnel junctions shows however a more multifaceted behavior. We find, in particular, that there is a sizable charge transfer from Cu to the interfacial monolayer of CrI_3 at the Cu/CrI_3 interface. This makes this CrI_3 monolayer "half-metallic", that is, such that the majority spins experience no barrier within this monolayer, whereas the minority spins encounter a tunnel barrier. Furthermore, the detailed analysis of the complex band structure of CrI_3 shows that the spin-filtering effect cannot be quantitatively understood based on a simple model of the spin-dependent barrier heights. The important roles are played by the $\mathbf{k}_{||}$- and spin-dependent evanescent states, their symmetries, and matching to the propagating states in the electrodes. These effects add new important features to the mechanism of spin filtering in CrI_3-based tunnel junctions. Our results provide important insights into the understanding of spin-filtering-produced FM insulators, such as CrI_3, and may be useful for the design of novel magnetoresistive devices based on 2D magnetic crystals.

METHODS

The atomic and electronic structure of the system is calculated using DFT as implemented in Vienna ab initio simulation package.[32,33] The projected augmented plane-wave (PAW) method is used to approximate the electron-ion potential.[34] The exchange-correlation potential is described within generalized density approximation. In the calculations, we use a kinetic energy cutoff of 340 eV for the plane-wave expansion of the PAWs and $6 \times 6 \times 1$ and grid of k points for the Brillouin zone integration. For the accurate description of the interlayer separation in CrI_3, the van der Waal's interaction is included in the calculations.[35] The in-plane lattice constant is fixed to the theoretical value of the bulk CrI_3 lattice constant of 6.81 Å, which is close to the experimental value of 6.88 Å. With this in-plane lattice constant, the out-of-plane lattice constant and all the internal coordinates of the supercells are relaxed until the Hellman−Feynman force on each atom is less than 0.01 eV/Å. Under these conditions, the interplane separation of the CrI_3 monolayers is found to be 6.45 Å. All the calculations are spin-polarized with the Cr moment aligned parallel within the CrI_3 monolayers. The FM (AFM) phase of CrI_3 is described by assuming parallel (antiparallel) alignment of the magnetic moments of the adjacent CrI_3 monolayers. For the AFM structure, three monolayers of CrI_3 are not compatible with the periodic boundary conditions, and hence, we increase the lattice by a factor of 2 in the c-direction. The band offset calculations are performed using a six-layer-thick Cu slab [equivalent to two unit cells of Cu(111)] padded with 16 Å vacuum and an eight-monolayer-thick AFM-ordered CrI_3 slab padded with 16 Å of vacuum. The work function is defined by the potential energy difference between the vacuum and the Fermi level for the Cu slab and the VBM for the CrI_3 slab.

The transmission and complex band structure calculations are carried out using the Atomistic Simulation Toolkit with the PBE pseudopotentials distributed in the QuantumWise package (Version 2015.1).[36,37] As implemented in the code, the transmission is calculated using the nonequilibrium Green's function approach.[38] The $Cu/CrI_3/Cu(111)$ supercell is used as the scattering region, ideally attached on both sides to semi-infinite Cu(111) leads.[35] This structure has open boundary conditions in the c-direction but is periodic in the a,b plane. The latter property makes the in-plane Bloch wave vector $\mathbf{k}_{||}$ a good quantum number so that transmission T is a function of $\mathbf{k}_{||}$. For calculating transmission, the 2D Brillouin zone is sampled using a uniform 51×51 $\mathbf{k}_{||}$ mesh.

The atomic structure of the $Cu/CrI_3/Cu(111)$ junctions is designed with the help of VNL distributed with Atomistic toolkit.[39]

ASSOCIATED CONTENT

Supporting Information

The Supporting Information is available free of charge on the ACS Publications website at DOI: 10.1021/acsami.9b01942.

Electronic and transport properties of a two-monolayer tunnel junction $Cu/CrI_3(2ML)/Cu$: layer- and spin-resolved DOS spin-resolved transmission as a function of energy for FM- and AFM-ordered CrI_3, and $\mathbf{k}_{||}$-resolved transmission in the 2D Brillouin zone for FM- and AFM-ordered CrI_3 (PDF)

AUTHOR INFORMATION

Corresponding Authors

*E-mail: tpaudel2@unl.edu (T.R.P.).
*E-mail: tsymbal@unl.edu (E.Y.T.).

ORCID

Tula R. Paudel: 0000-0002-9952-9435
Evgeny Y. Tsymbal: 0000-0002-6728-5480

Notes

The authors declare no competing financial interest.

ACKNOWLEDGMENTS

The authors thank Dr. Lingling Tao for valuable discussions. This research was supported by the Semiconductor Research Corporation (SRC) through the nCORE program and the National Science Foundation (NSF) through the E2CDA program (grant ECCS-1740136). Computations were performed at the University of Nebraska Holland Computing Center. The atomic structure was produced using VESTA software.[40]

REFERENCES

(1) Geim, A. K.; Grigorieva, I. V. Van der Waals heterostructures. *Nature* **2013**, *499*, 419−425.
(2) Novoselov, K. S.; Mishchenko, A.; Carvalho, A.; Castro Neto, A. H. 2D Materials and van der Waals heterostructures. *Science* **2016**, *353*, aac9439.
(3) Huang, B.; Clark, G.; Navarro-Moratalla, E.; Klein, D. R.; Cheng, R.; Seyler, K. L.; Zhong, D.; Schmidgall, E.; McGuire, M. A.; Cobden, D. H.; Yao, W.; Xiao, D.; Jarillo-Herrero, P.; Xu, X. -dependent ferromagnetism in a van der Waals crystal down to the monolayer limit. *Nature* **2017**, *546*, 270−273.
(4) Gong, C.; Li, L.; Li, Z.; Ji, H.; Stern, A.; Xia, Y.; Cao, T.; Bao, W.; Wang, C.; Wang, Y.; Qiu, Z. Q.; Cava, R. J.; Louie, S. G.; Xia, J.; Zhang, X. Discovery of intrinsic ferromagnetism in two-dimensional van der Waals crystals. *Nature* **2017**, *546*, 265−269.
(5) Bonilla, M.; Kolekar, S.; Ma, Y.; Diaz, H. C.; Kalappattil, V.; Das, R.; Eggers, T.; Gutierrez, H. R.; Phan, M.-H.; Batzill, M. Strong room-temperature ferromagnetism in VSe2 monolayers on van der Waals substrates. *Nat. Nanotechnol.* **2018**, *13*, 289−293.
(6) Mermin, N. D.; Wagner, H. Absence of ferromagnetism or antiferromagnetism in one- or two-dimensional isotropic Heisenberg models. *Phys. Rev. Lett.* **1966**, *17*, 1307.
(7) Zhang, W.-B.; Qu, Q.; Zhu, P.; Lam, C.-H. Robust intrinsic ferromagnetism and half semiconductivity in stable two-dimensional single-layer chromium trihalides. *J. Mater. Chem. C* **2015**, *3*, 12457−12468.
(8) McGuire, M. A.; Dixit, H.; Cooper, V. R.; Sales, B. C. Coupling of Crystal Structure and Magnetism in the Layered, Ferromagnetic Insulator CrI3. *Chem. Mater.* **2015**, *27*, 612−620.

DOI: 10.1021/acsami.9b01942
ACS Appl. Mater. Interfaces 2019, 11, 15781−15787

(9) Dillon, J. F.; Olson, C. E. Magnetization, Resonance, and Optical Properties of the Ferromagnet CrI3. *J. Appl. Phys.* **1965**, *36*, 1259−1260.
(10) Lado, J. L.; Fernández-Rossier, J. On the origin of magnetic anisotropy in two dimensional CrI3. *2D Mater* **2017**, *4*, 035002.
(11) Sivadas, N.; Okamoto, S.; Xiao, D. Gate-controllable magneto-optic Kerr effect in layered collinear antiferromagnets. *Phys. Rev. Lett.* **2016**, *117*, 1−5.
(12) Jiang, S.; Li, L.; Wang, Z.; Mak, K. F.; Shan, J. Controlling magnetism in 2D CrI3 by electrostatic doping. *Nat. Nanotechnol.* **2018**, *13*, 549−553.
(13) Jiang, S.; Shan, J.; Mak, K. F. Electric-field switching of two-dimensional van der Waals magnets. *Nat. Mater.* **2018**, *17*, 406−410.
(14) Huang, B.; Clark, G.; Klein, D. R.; Macneill, D.; Navarro-Moratalla, E.; Seyler, K. L.; Wilson, N.; McGuire, M. A.; Cobden, D. H.; Xiao, D.; Yao, W.; Jarillo-Herrero, P. Electrical control of 2D magnetism in bilayer CrI3. *Nat. Nanotechnol.* **2018**, *13*, 544−548.
(15) Klein, D. R.; MacNeill, D.; Lado, J. L.; Soriano, D.; Navarro-Moratalla, E.; Watanabe, K.; Taniguchi, T.; Manni, S.; Canfield, P.; Fernández-Rossier, J.; Jarillo-Herrero, P. Probing magnetism in 2D van der Waals crystalline insulators via electron tunneling. *Science* **2018**, *360*, 1218−1222.
(16) Tsymbal, E. Y.; Mryasov, O. N.; LeClair, P. R. Spin-dependent tunnelling in magnetic tunnel junctions. *J. Phys. Condens. Matter* **2003**, *15*, R109−R142.
(17) Zhuravlev, M. Y.; Maekawa, S.; Tsymbal, E. Y. Effect of spin-dependent screening on tunneling electroresistance and tunneling magnetoresistance in multiferroic tunnel junctions. *Phys. Rev. B: Condens. Matter Mater. Phys.* **2010**, *81*, 104419.
(18) Velev, J. P.; Burton, J. D.; Zhuravlev, M. Y.; Tsymbal, E. Y. Predictive modelling of ferroelectric tunnel junctions. *npj Comp. Mater.* **2016**, *2*, 16009.
(19) Song, T.; Cai, X.; Tu, M. W.-Y.; Zhang, X.; Huang, B.; Wilson, N. P.; Seyler, K. L.; Zhu, L.; Taniguchi, T.; Watanabe, K.; Mcguire, M. A.; Cobden, D. H.; Xiao, D.; Yao, W.; Xu, X. Giant tunneling magnetoresistance in spin-filter van der Waals heterostructures. *Science* **2018**, *360*, 1214−1218.
(20) Wang, Z.; Gutiérrez-Lezama, I.; Ubrig, N.; Kroner, M.; Gibertini, M.; Taniguchi, T.; Watanabe, K.; Imamoğlu, A.; Giannini, E.; Morpurgo, A. F. Very large tunneling magnetoresistance in layered magnetic semiconductor CrI_3. *Nat. Commun.* **2018**, *9*, 2516.
(21) Kim, H. H.; Yang, B.; Patel, T.; Sfigakis, F.; Li, C.; Tian, S.; Lei, H.; Tsen, A. W. One million percent tunnel magnetoresistance in a magnetic van der Waals heterostructure. *Nano Lett.* **2018**, *18*, 4885−4890.
(22) Wang, H.; Eyert, V.; Schwingenschlögl, U. Electronic structure and magnetic ordering of the semiconducting chromium trihalides CrCl3, CrBr3, and CrI3. *J. Phys. Condens. Matter* **2011**, *23*, 116003.
(23) Santos, T.; Moodera, J. Spin-filter tunneling. In *Handbook of Spin Transport and Magnetism*; Tsymbal, E. Y., Žutić, I., Eds.; CRC Press, 2012, Chapter 13, pp. 251−266.
(24) Lukashev, P. V.; Burton, J. D.; Smogunov, A.; Velev, J. P.; Tsymbal, E. Y. Interface states in $CoFe_2O_4$ spin-filter tunnel junctions. *Phys. Rev. B* **2017**, *88*, 134430.
(25) Approximating the exchange-correlation potential with a semi-local functional, such as HSE, overestimates the band gap up to about 1.6 eV. See, e.g., Heyd, J.; Scuseria, G. E.; Ernzerhof, M. Hybrid functionals based on a screened Coulomb potential. *J. Chem. Phys.* **2003**, *118*, 8207−8215; Erratum: "Hybrid functionals based on a screened Coulomb potential" [J. Chem. Phys. 118, 8207 (2003)]. **2006**, *124*, 219906. Krukau, A. V.; Vydrov, O. A.; Izmaylov, A. F.; Scuseria, G. E. Influence of the exchange screening parameter on the performance of screened hybrid functionals. *J. Chem. Phys* **2006**, *125*, 224106.
(26) Jelver, L.; Larsen, P. M.; Stradi, D.; Stokbro, K.; Jacobsen, K. W. Determination of low-strain interfaces via geometric matching. *Phys. Rev. B* **2017**, *96*, 085306.
(27) See the Supporting Information.
(28) Heine, V. On the general theory of surface states and scattering of electrons in solids. *Proc. Phys. Soc.* **1963**, *81*, 300−310; Theory of surface states. *Phys. Rev.* **1965**, *138*, A1689−A1696.
(29) Mavropoulos, P.; Papanikolaou, N.; Dederichs, P. H. Complex band structure and tunneling through ferromagnet/insulator/ferromagnet junctions. *Phys. Rev. Lett.* **2000**, *85*, 1088−1091.
(30) Velev, J. P.; Belashchenko, K. D.; Jaswal, S. S.; Tsymbal, E. Y. Effect of oxygen vacancies on spin-dependent tunneling in Fe/MgO/Fe magnetic tunnel junctions. *Appl. Phys. Lett.* **2007**, *90*, 072502.
(31) Lukashev, P.; Wysocki, A.; Velev, J. P.; van Schilfgaarde, M.; Jaswal, S. S.; Belashchenko, K. D.; Tsymbal, E. Y. Spin filtering with EuO: Insight from a complex band structure. *Phys. Rev. B: Condens. Matter Mater. Phys.* **2012**, *85*, 224414.
(32) Kresse, G.; Joubert, D. From ultrasoft pseudopotentials to the projector augmented-wave method. *Phys. Rev. B* **1999**, *59*, 1758−1775.
(33) Kresse, G.; Furthmüller, J. Efficient iterative schemes forab initiototal-energy calculations using a plane-wave basis set. *Phys. Rev. B: Condens. Matter Mater. Phys.* **1996**, *54*, 11169−11186.
(34) Blöchl, P. E. Projector augmented-wave method. *Phys. Rev. B: Condens. Matter Mater. Phys.* **1994**, *50*, 17953−17979.
(35) Grimme, S.; Antony, J.; Ehrlich, S.; Krieg, H. A consistent and accurate ab initio parametrization of density functional dispersion correction (DFT-D) for the 94 elements H-Pu. *J. Chem. Phys.* **2010**, *132*, 154104. Grimme, S.; Ehrlich, S.; Goerigk, L. Effect of the damping function in dispersion corrected density functional theory. *J. Comput. Chem.* **2011**, *32*, 1456−1465.
(36) Brandbyge, M.; Mozos, J.-L.; Ordejón, P.; Taylor, J.; Stokbro, K. Density-functional method for nonequilibrium electron transport. *Phys. Rev. B: Condens. Matter Mater. Phys.* **2002**, *65*, 165401.
(37) Soler, J. M.; Artacho, E.; Gale, J. D.; García, A.; Junquera, J.; Ordejón, P.; Sánchez-Portal, D. The SIESTA method forab initioorder-Nmaterials simulation. *J. Phys. Condens. Matter* **2002**, *14*, 2745−2779.
(38) Taylor, J.; Guo, H.; Wang, J. *Ab Initio* modeling of quantum transport properties of molecular electronic devices. *Phys. Rev. B: Condens. Matter Mater. Phys.* **2001**, *63*, 245407.
(39) *Atomistix Toolkit version 2015.1., Synopsys QuantumWise A/S* (www.quantumwise.com).
(40) Momma, K.; Izumi, F. VESTA 3for three-dimensional visualization of crystal, volumetric and morphology data. *J. Appl. Crystallogr.* **2011**, *44*, 1272−1276.

DOI: 10.1021/acsami.9b01942
ACS Appl. Mater. Interfaces 2019, 11, 15781−15787